A&A 546, A55 (2012)
DOI: 10.1051/0004-6361/201220014

Astronomy & Astrophysics

Stellar laboratories: new Ge V and Ge VI oscillator strengths and their validation in the hot white dwarf RE 0503–289⋆,⋆⋆,⋆⋆⋆

T. Rauch[1], K. Werner[1], É. Biémont[2,3], P. Quinet[2,3], and J. W. Kruk[4]

[1] Institute for Astronomy and Astrophysics, Kepler Center for Astro and Particle Physics, Eberhard Karls University, Sand 1, 72076 Tübingen, Germany
e-mail: rauch@astro.uni-tuebingen.de
[2] Astrophysique et Spectroscopie, Université de Mons – UMONS, 7000 Mons, Belgium
[3] IPNAS, Université de Liège, Sart Tilman, 4000 Liège, Belgium
[4] NASA Goddard Space Flight Center, Greenbelt, MD 20771, USA

Received 13 July 2012 / Accepted 14 August 2012

ABSTRACT

Context. State-of-the-art spectral analysis of hot stars by means of non-LTE model-atmosphere techniques has arrived at a high level of sophistication. The analysis of high-resolution and high-S/N spectra, however, is strongly restricted by the lack of reliable atomic data for highly ionized species from intermediate-mass metals to trans-iron elements. Especially data for the latter has only been sparsely calculated. Many of their lines are identified in spectra of extremely hot, hydrogen-deficient post-AGB stars. A reliable determination of their abundances establishes crucial constraints for AGB nucleosynthesis simulations and, thus, for stellar evolutionary theory.

Aims. In a previous analysis of the UV spectrum of RE 0503−289, spectral lines of highly ionized Ga, Ge, As, Se, Kr, Mo, Sn, Te, I, and Xe were identified. Individual abundance determinations are hampered by the lack of reliable oscillator strengths. Most of these identified lines stem from Ge V. In addition, we identified Ge VI lines for the first time. We calculated Ge V and Ge VI oscillator strengths in order to reproduce the observed spectrum.

Methods. We newly calculated Ge V and Ge VI oscillator strengths to consider their radiative and collisional bound-bound transitions in detail in our non-LTE stellar-atmosphere models for the analysis of the Ge IV–VI spectrum exhibited in high-resolution and high-S/N FUV (FUSE) and UV (ORFEUS/BEFS, IUE) observations of RE 0503−289.

Results. In the UV spectrum of RE 0503−289, we identify four Ge IV, 37 Ge V, and seven Ge VI lines. Most of these lines are identified for the first time in any star. We can reproduce almost all Ge IV, Ge V, and Ge VI lines in the observed spectrum of RE 0503−289 ($T_{\rm eff}$ = 70 kK, $\log g$ = 7.5) at $\log$ Ge = −3.8 ± 0.3 (mass fraction, about 650 times solar). The Ge IV/V/VI ionization equilibrium, that is a very sensitive $T_{\rm eff}$ indicator, is reproduced well.

Conclusions. Reliable measurements and calculations of atomic data are a prerequisite for stellar-atmosphere modeling. Our oscillator-strength calculations have allowed, for the first time, Ge V and Ge VI lines to be successfully reproduced in a white dwarf's (RE 0503−289) spectrum and to determine its photospheric Ge abundance.

Key words. atomic data – line: identification – stars: abundances – stars: individual: RE0503-289 – white dwarfs – virtual observatory tools

1. Introduction

Any model-atmosphere calculation is strongly dependent on the available and reliable atomic data, which is a crucial input. Especially for highly ionized species and higher atomic mass, published data becomes rather sparse. A close inspection of the UV spectrum of the hot white dwarf RE 0503−289 by Werner et al. (2012) has shown that a large number of the hitherto unidentified observed spectral lines stem from trans-iron elements, namely Ga, Ge, As, Se, Mo, Sn, Te, and I.

Identification of the respective spectral lines is fairly straightforward because atomic databases like NIST[1] and Kelly's database[2] have partly included the strongest lines of these elements with accurate wavelengths, whereas a quantitative analysis requires adequate spectral modeling. This is hampered by the fact that line strengths for trans-iron elements, when available at all, are relative intensities measured from emission line spectra. Exploratory atmosphere models that are based on the LTE assumption to calculate occupation numbers of the atomic levels of an ion and on $\log gf$ values scaled to match the relative line strengths may show that the line identifications are correct. A reliable abundance analysis, however, is impossible owing to the lack of measured or calculated transition probabilities.

The line identification was demonstrated by Werner et al. (2012) in the case of RE 0503−289. It is a hot ($T_{\rm eff}$ = 70 kK, $\log g$ = 7.5), helium-rich DO-type white dwarf (WD 0501−289, $\alpha_{2000} = 05^{\rm h}03^{\rm m}55\overset{\rm s}{.}513$, $\delta_{2000} = -28°54'34\overset{''}{.}57$), which is well-suited to UV spectroscopy because its spectrum is only slightly contaminated by interstellar absorption. Werner et al. (2012) performed an abundance analysis of Kr and Xe where level energies

⋆ Based on observations made with the NASA-CNES-CSA Far Ultraviolet Spectroscopic Explorer.
⋆⋆ Figures 4–6 and Tables 1, 3 are available in electronic form at http://www.aanda.org
⋆⋆⋆ Tables 2 and 4 are only available at the CDS via anonymous ftp to cdsarc.u-strasbg.fr (130.79.128.5) or via http://cdsarc.u-strasbg.fr/viz-bin/qcat?J/A+A/546/A55

[1] http://www.nist.gov/pml/data/asd.cfm
[2] http://www.cfa.harvard.edu/ampcgi/kelly.pl

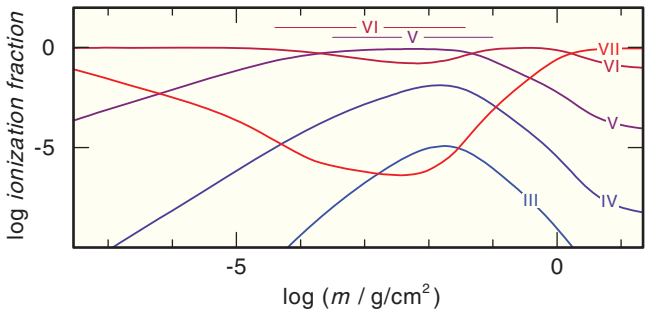

Fig. 1. Ionization fractions of Ge III–VII. The formation depths of the Ge V and Ge VI line cores are marked at the top.

and oscillator strengths of Kr VI, Kr VII, Xe VI, and Xe VII were already published. They determined log Kr = −4.3 ± 0.5 and log Xe = −4.2 ± 0.6 (mass fractions) and identified a variety of lines of the other trans-iron elements mentioned above.

Only level energies and (partly) relative line strengths were accessible for Ge. A test calculation of an H+Ge-composed model atmosphere with the relevant parameters ($T_{\rm eff}$ = 70 kK, log g = 7.5), log Ge = −4) shows that Ge V and Ge VI are dominant in the line-forming region (Fig. 1). Consequently, we calculated transition probabilities anew for Ge V and Ge VI (Sect. 2). In Sect. 3, we briefly introduce the available observed spectra, which are used for our Ge abundance analysis of RE 0503−289 that is presented in Sect. 4. In Sect. 5 we re-assess the effective temperature of RE 0503−289 based on the C III / C IV ionization balance. Results and conclusions are summarized in Sect. 6.

2. Transition probabilities in Ge V and Ge VI

There are not very many transition probabilities or oscillator strengths in Ge V and Ge VI ions. In Ge V, some pioneering HFR[3] and MCDF[4] (Grant & McKenzie 1980; Grant et al. 1980) results were reported by Quinet & Biémont (1990, 1991) but the work of these authors was limited to 3d–4p and 3d–4f transitions in nickel-like ions (Ge V–Pb LV). More recent work comes from Safronova and co-workers (Safronova et al. 2000; Hamasha et al. 2004; Safronova et al. 2006a,b; Safronova & Safronova 2006), who performed relativistic many-body calculations for multipole transitions (E1, M1, E2, M2, E3, M3) originating in the ground states.

In Ge VI, the available results are limited to forbidden transitions in 3d and $3d^9$ configurations (Biémont & Hansen 1989) and to the theoretical investigation of electric dipole transitions between $3d^9$ and d^8p configurations in zinc, gallium, and germanium ions (Jucys et al. 1968).

As there is no uniform set of oscillator strengths available for all the transitions of Ge ions observed in the present work, we decided to perform the relevant calculations. The method adopted here is the relativistic Hartree-Fock approach frequently referred to in the literature as the HFR or Cowan's method (Cowan 1981).

For Ge V, configuration interaction has been considered among the configurations $3d^{10}$, $3d^9ns$ (n = 4–7), $3d^9nd$ (n = 4–7), $3d^84s^2$, $3d^84p^2$, $3d^84d^2$, $3d^84f^2$, $3d^84sns$ (n = 5–7), $3d^84snd$ (n = 4–7), and $3d^84p4f$ for the even parity, and $3d^9np$ (n = 4–7), $3d^9nf$ (n = 4–7), $3d^84snp$ (n = 4–7), $3d^84snf$ (n = 4–7), and $3d^84p4d$ for the odd parity. Using experimental energy levels reported by Sugar & Musgrove (1993) and Churilov et al. (1997), the radial integrals (average energies, Slater integrals, spin-orbit parameters) of $3d^{10}$, $3d^9ns$ (n = 4–7), $3d^9np$ (n = 4–6), $3d^9nd$ (n = 4,5), $3d^94f$ and $3d^84s4p$ were optimized by a well-established least-squares fitting procedure. In this process, the $3d^94d\ ^1S_0$ level at 493 765.5 cm^{-1} (Sugar & Musgrove 1993) and the $3d^84s4p$ (J = 1) level at 673 405 cm^{-1} (Churilov et al. 1997), affected by larger uncertainties, were not considered.

For Ge VI, the configurations included in the HFR model were $3d^9$, $3d^84s$, $3d^85s$, $3d^84d$, $3d^85d$, $3d^74s^2$, $3d^74p^2$, $3d^74d^2$, $3d^74f^2$, $3d^74s5s$, $3d^74s4d$, and $3d^74s5d$ for the even parity and $3d^84p$, $3d^85p$, $3d^84f$, $3d^85f$, $3d^74s4p$, $3d^74s5p$, $3d^74s4f$, $3d^74s5f$, and $3d^74p4d$ for the odd parity. In this case, the semi-empirical process was performed to optimize the radial integrals corresponding to $3d^9$, $3d^84s$, and $3d^84p$ configurations using the experimental levels reported by Sugar & Musgrove (1993). The $3d^94f$ levels were excluded from the fit because many of these were found to be mixed with experimentally unknown levels belonging notably to the $3d^95p$ configuration.

The experimental and calculated energy levels for Ge V, expressed in cm^{-1}, are reported in Table 1 which also shows the differences between both sets of results (ΔE) and, in the last column, the percentage composition in LS-coupling (only the first three components over 5% are given). This last piece of information is useful because oscillator strengths for transitions connecting strongly perturbed levels are more sensitive to configuration interaction effects.

The calculated HFR oscillator strengths on a logarithmic scale (log gf) and transition probabilities (gA, in s^{-1}) for Ge V are reported in Table 2 with the corresponding wavelengths (in Å) and energy levels (in cm^{-1}). In the last column, we give the cancellation factor CF as defined by Cowan (1981). Low values of this factor indicate strong cancellation effects in the calculations. The corresponding transition probabilities could be very inaccurate so need to be considered with some care. It does appear, however, from the last column of the table that very few transitions are affected by such effects.

The experimental and calculated energy levels for Ge VI appear in Table 3 and the corresponding calculated HFR oscillator strengths and transition probabilities are reported in Table 4. Here too, very few transitions are affected by cancellation effects so that for most of the transitions, the f values should be reliable.

3. Observations

For our analysis, we mainly use the FUSE spectrum of RE 0503−289 that is described in detail by Werner et al. (2012). In addition, we use UV spectra that were obtained with ORFEUS[5]/BEFS[6], ORFEUS/GHRS[7] and IUE[8]. The BEFS spectrum (909–1222 Å) is co-added from five observations (ObsIds: BEFS2003, BEFS2126, BEFS2128, BEFS2133, BEFS2173; with a total observation time of 6826 s). The GHRS spectrum (1228–1275 Å, 1339–1375 Å, 1610–1655 Å) is co-added from eight observations (ObsIds: Z3GM0204T, Z3GM0205T, Z3JU0104T, Z3JU0107T, Z3JU0108T, Z3JU0109T, Z3JU010AT, Z3JU010BT; 5155 s). The IUE spectrum (1153–1947 Å) is the co-added spectrum (ObsIds: SWP46428, SWP49788, SWP52796, SWP52803;

[3] Hartree-Fock with relativistic corrections.
[4] Multi-Configuration Dirac-Fock.
[5] Orbiting Retrievable Far and Extreme Ultraviolet Spectrometer.
[6] Berkeley Extreme and Far-UV Spectrometer.
[7] Goddard High-Resolution Spectrograph.
[8] International Ultraviolet Explorer.

Table 5. Statistics of the Ge model atom used in our calculations.

Ion	Levels		Line transitions		
	NLTE	LTE	total	known f	unknown f
III	14	2	0		
IV	8	1	8	8	
V	85	0	1345	878	467
VI	36	0	235	160	75
VII	1	0	0		

136 193 s) provided by the IUE NEWSIPS data base[9] (Holberg et al. 1998).

Optical spectra were taken in the framework of the SPY[10] project (Napiwotzki et al. 2001, 2003) with UVES[11] at ESO's[12] VLT[13].

4. The photospheric Ge abundance in RE 0503−289

Ge V and Ge VI are the dominant ionization stages in the line-forming region of RE 0503−289 (Fig. 1). Thus, we constructed a Ge III–VII model atom (Table 5, Fig. 2). We used level energies from NIST for all ions. For Ge IV, we considered the oscillator strengths of Nath Dutta & Majumder (2011) and, where missing, approximated values from the isoelectronic C IV. Ge V and Ge VI include our newly calculated oscillator strengths (Sect. 2). Analogously to Werner et al. (2012) in the case of Kr and Xe, the unknown f values (Table 5) of these two ions were set to 10^{-4} within a spin and to 10^{-6} otherwise. Test calculations have shown that the Ge line profiles in the UV do not change when we set $f = 0$ for these lines. Photoionization rates were computed with hydrogen-like crosssections. Electron collisional excitation and ionization rates were evaluated with the usual approximation formulae following van Regemorter (1962) and Seaton (1962), respectively. This enabled us to build on the HeCNOKrXe models for RE 0503−289 described by Werner et al. (2012) and to consider Ge opacities as well as iron-group opacities (elements Ca-Ni, own determination of upper abundance limits) in addition. Compared to Werner et al. (2012), we reduced the N abundance to match the N IV 2p ^{3}P^o–2p^2 ^{3}P multiplet (921–924 Å, Fig. 3).

We used the Tübingen Model-Atmosphere Package (TMAP[14] Werner et al. 2003) to calculate state-of-the-art, plane-parallel, chemically homogeneous model atmospheres in hydrostatic and radiative equilibrium. The considered model atoms are those that are provided via the Tübingen Model-Atom Database (TMAD[15], Rauch & Deetjen 2003).

We compared the available UV spectra of RE 0503−289 (Sect. 3) with our TMAP model (and wavelength positions given by NIST and Kelly's database) in order to identify Ge lines. The line lists in that energy region, especially for the highly ionized trans-iron elements that are encountered, are rather incomplete, and thus, lines that are not considered in the models may contribute to the assumed isolated Ge lines. Ga V $\lambda\lambda$ 1054.560, 1069.450 Å are two examples (Fig. 3). The consideration of Ga in the model-atmosphere calculation would

[9] http://vega.lpl.arizona.edu/newsips/
[10] ESO SN Ia Progenitor surveY.
[11] Ultraviolet and Visual Echelle Spectrograph.
[12] http://www.eso.org/public/
[13] Very Large Telescope.
[14] http://astro.uni-tuebingen.de/~TMAP
[15] http://astro.uni-tuebingen.de/~TMAD

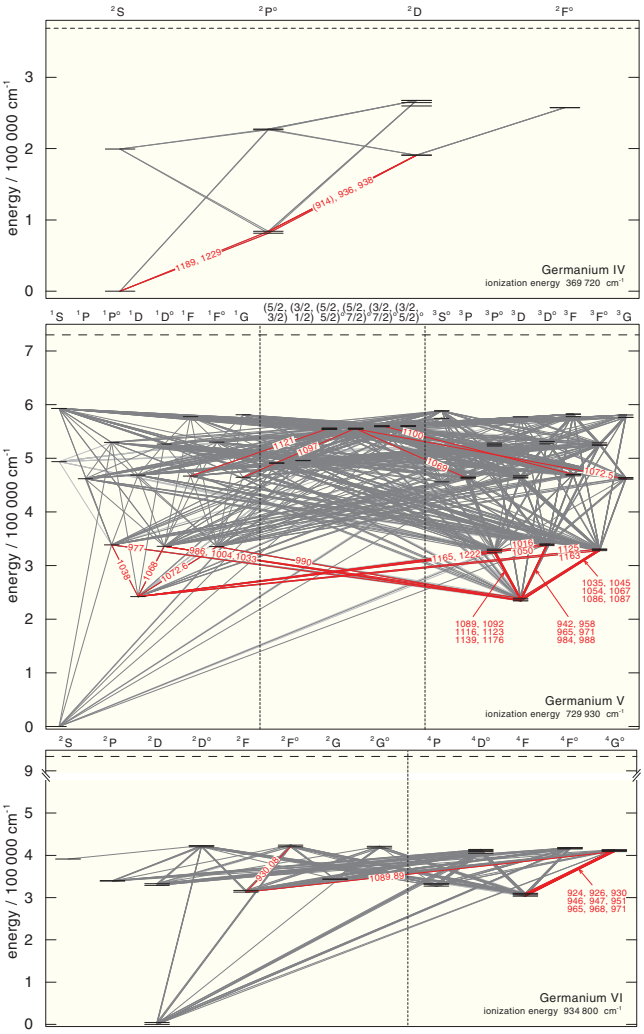

Fig. 2. Grotrian diagram of our Ge IV (*top*), Ge V (*middle*), and Ge VI (*bottom*) model ions. Thick black and thin gray lines represent radiative transitions with known and unknown f values, respectively. The identified lines (red) are labeled with their respective wavelengths in Å.

improve the fit of the blends with Ge V $\lambda\lambda$ 1054.588, 1069.419 Å. However, we identify four Ge IV, 37 Ge V, and six Ge VI lines (Table 6). All Ge IV and Ge V lines are in general reproduced in both strength and width by our model simultaneously at log Ge = −3.81 ± 0.3 (Fig. 3). There is only one line, Ge V λ 1123.744 Å, that is much too strong in our model. The reason is unknown. The Ge VI lines are weak in our model and just emerge from the noise in the FUSE observation, but they do agree. Ge VI $\lambda\lambda$ 986.721, 1039.890 Å are too weak to reproduce the observed absorption features, most likely due to unknown blends at their positions that are not considered in the model. However, the large number of identified Ge lines and their modeling give convincing evidence that our model and the determined Ge abundance are realistic.

5. Effective temperature and surface gravity of RE 0503−289

Both $T_{\rm eff}$ and log g were adopted from Werner et al. (2012) for this analysis. Figure 3 shows that the C III multiplet 2p ^{3}P^o–2p^2 ^{3}P (1174–1176 Å) in our model is too weak. Since an

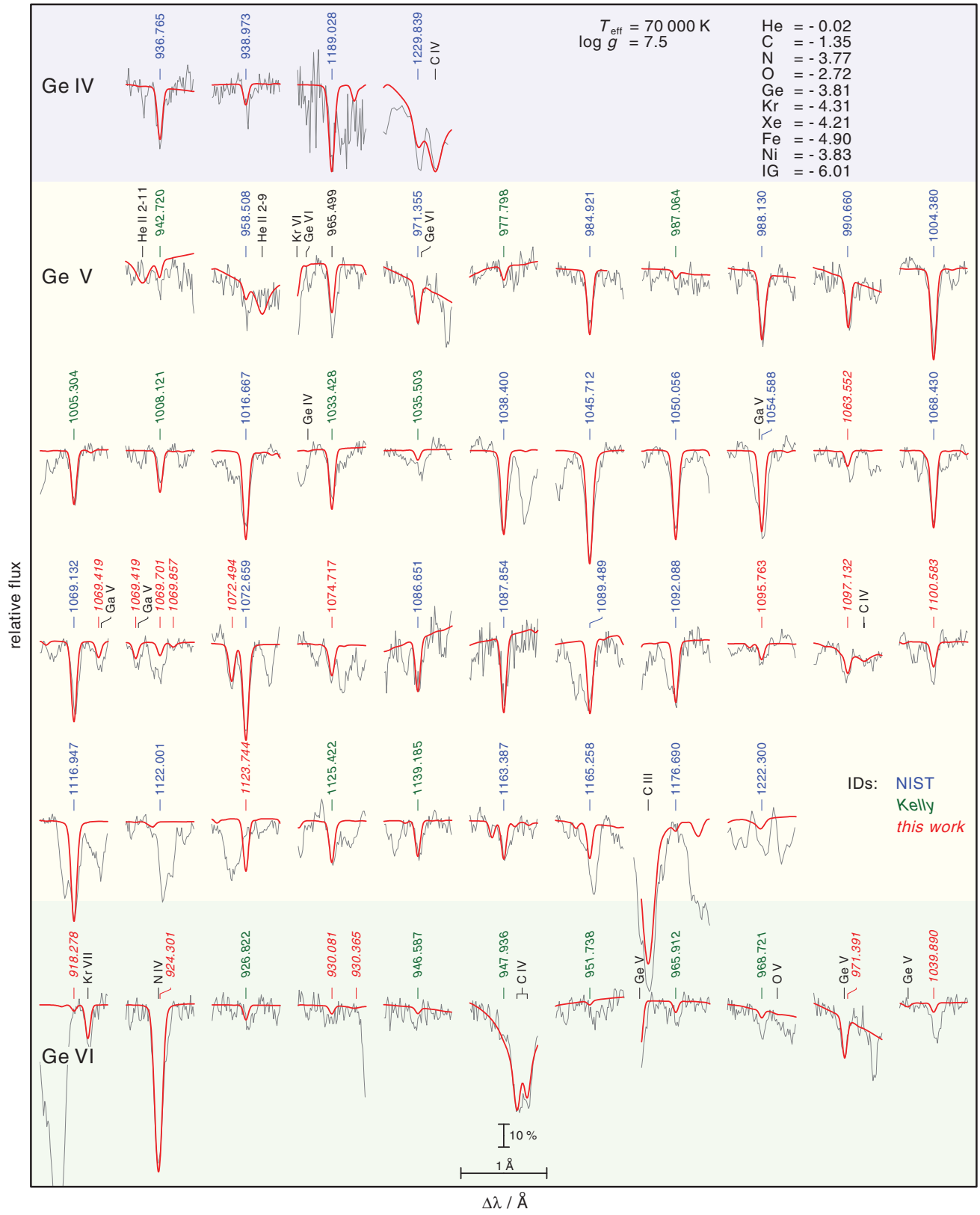

Fig. 3. Ge IV (*top*), Ge V, and Ge VI (*bottom*) lines in FUSE, ORFEUS/BEFS (Ge IV λ 1189 Å), and IUE (Ge V λ 1222 Å, Ge IV λ 1229 Å) observations compared with a $T_{\rm eff}$ = 70 kK/log g = 7.5 TMAP model. The abundances (*top right*) are logarithmic mass fractions. IG denotes a generic model atom (Rauch & Deetjen 2003), which comprises Ca, Sc, Ti, V, Cr, Mn, and Co. The synthetic spectra a convolved with a Gaussian of 0.05 Å (*FWHM*, 0.1 Å for the IUE comparison) to match the instrument resolution. A radial-velocity shift of $v_{\rm rad}$ = 23 km s^{-1} is applied to the observation.

Table 6. Identified Ge lines in the UV spectrum of RE 0503−289.

Ion	Lower level	Upper level	f value	Wavelength / Å		Comment
Ge IV	$4p\ ^2P^o_{3/2}$	$4d\ ^2D_{5/2}$	8.91E-01	936	765	
	$4p\ ^2P^o_{3/2}$	$4d\ ^2D_{3/2}$	9.89E-02	938	973	
	$4s\ ^2S_{1/2}$	$4p\ ^2P^o_{3/2}$	5.54E-01	1189	028	
	$4s\ ^2S_{1/2}$	$4p\ ^2P^o_{1/2}$	2.66E-01	1229	839	
Ge V	$4s\ ^3D_3$	$4p\ ^3D^o_2$	8.22E-03	942	720	
	$4s\ ^3D_2$	$4p\ ^3D^o_2$	3.17E-02	958	508	
	$4s\ ^3D_2$	$4p\ ^3D^o_1$	3.56E-02	965	499	
	$4s\ ^3D_3$	$4p\ ^3D^o_3$	1.22E-01	971	355	
	$4s\ ^3D_2$	$4p\ ^1P^o_1$	3.56E-03	977	798	Kelly wavelength
	$4s\ ^3D_1$	$4p\ ^3D^o_2$	1.08E-01	984	921	
	$4s\ ^3D_3$	$4p\ ^1D^o_2$	1.13E-03	987	064	Kelly wavelength
	$4s\ ^3D_2$	$4p\ ^3D^o_3$	1.00E-01	988	130	
	$4s\ ^3D_3$	$4p\ ^1F^o_3$	1.13E-01	990	660	
	$4s\ ^3D_2$	$4p\ ^1D^o_2$	1.70E-01	1004	380	NIST wavelength
	$4s\ ^3D_1$	$4p\ ^1P^o_1$	5.41E-02	1005	304	Kelly wavelength
	$4s\ ^3D_2$	$4p\ ^1F^o_3$	1.21E-02	1008	121	
	$4s\ ^1D_2$	$4p\ ^3D^o_2$	1.95E-01	1016	667	
	$4s\ ^3D_1$	$4p\ ^1D^o_2$	6.96E-02	1033	428	Kelly wavelength
	$4s\ ^3D_3$	$4p\ ^3F^o_2$	1.01E-03	1035	503	
	$4s\ ^1D_2$	$4p\ ^1P^o_1$	1.45E-01	1038	400	NIST wavelength
	$4s\ ^3D_3$	$4p\ ^3F^o_4$	3.94E-01	1045	712	
	$4s\ ^1D_2$	$4p\ ^3D^o_3$	1.56E-01	1050	056	
	$4s\ ^3D_2$	$4p\ ^3F^o_2$	8.93E-02	1054	588	
	$4d\ ^3P_1$	$4f\ ^5F^o_2$	8.57E-01	1063	552	
	$4s\ ^1D_2$	$4p\ ^1D^o_2$	8.73E-02	1068	430	NIST wavelength
	$4s\ ^3D_3$	$4p\ ^3F^o_3$	6.53E-02	1069	132	NIST wavelength
	$4d\ ^3P_2$	4f	5.02E-01	1069	419	
	$4d\ ^1P_1$	4f	6.07E-01	1069	701	
	$4d\ ^3P_2$	4f	1.10E-01	1069	857	
	$4d\ ^3G_5$	4f	9.97E-01	1072	494	
	$4s\ ^1D_2$	$4p\ ^1F^o_3$	2.52E-01	1072	659	
	$4d\ ^3G_4$	4f	9.68E-01	1074	717	
	$4s\ ^3D_1$	$4p\ ^3F^o_2$	3.18E-01	1086	651	
	$4s\ ^3D_2$	$4p\ ^3F^o_3$	3.03E-01	1087	854	
	$4s\ ^3D_2$	$4p\ ^3P^o_1$	1.42E-01	1089	489	
	$4s\ ^3D_1$	$4p\ ^3P^o_0$	1.01E-01	1092	088	
	$4d\ ^3G_3$	$4f\ ^5D^o_3$	1.53E-02	1095	763	
	$4d\ ^1G_4$	4f	7.69E-01	1097	132	
	$4d\ ^3F_3$	4f	9.01E-01	1100	583	
	$4s\ ^3D_3$	$4p\ ^3P^o_2$	1.97E-01	1116	947	
	$4d\ ^1F_3$	4f	9.44E-02	1122	001	NIST wavelength, very weak
	$4s\ ^3D_1$	$4p\ ^3P^o_1$	3.83E-02	1123	744	
	$4s\ ^1D_2$	$4p\ ^3F^o_2$	1.29E-02	1125	422	
	$4s\ ^3D_2$	$4p\ ^3P^o_2$	9.14E-03	1139	185	
	$4s\ ^1D_2$	$4p\ ^3F^o_3$	1.29E-02	1163	387	
	$4s\ ^1D_2$	$4p\ ^3P^o_1$	1.48E-02	1165	258	
	$4s\ ^3D_1$	$4p\ ^3P^o_2$	2.06E-03	1176	690	C III blend
	$4s\ ^1D_2$	$4p\ ^3P^o_2$	4.91E-03	1222	300	
Ge VI	$4s\ ^4F_{7/2}$	$4p\ ^4G^o_{9/2}$	2.34E-04	918	278	
	$4s\ ^4F_{9/2}$	$4p\ ^4G^o_{7/2}$	2.34E-04	924	301	N IV blend
	$4s\ ^4F_{9/2}$	$4p\ ^4G^o_{11/2}$	3.63E-01	926	822	
	$4s\ ^2F_{7/2}$	$4p\ ^2F^o_{7/2}$	2.43E-01	930	081	
	$4s\ ^4F_{7/2}$	$4p\ ^4G^o_{5/2}$	8.07E-04	930	365	
	$4s\ ^4F_{7/2}$	$4p\ ^4G^o_{7/2}$	1.28E-01	946	587	
	$4s\ ^4F_{9/2}$	$4p\ ^4G^o_{9/2}$	1.15E-01	947	936	C IV blend
	$4s\ ^4F_{5/2}$	$4p\ ^4G^o_{5/2}$	1.03E-01	951	738	
	$4s\ ^4F_{3/2}$	$4p\ ^4G^o_{5/2}$	2.62E-01	965	912	
	$4s\ ^4F_{5/2}$	$4p\ ^4G^o_{7/2}$	1.96E-01	968	721	
	$4s\ ^4F_{7/2}$	$4p\ ^4G^o_{9/2}$	1.81E-01	971	391	
	$4s\ ^2F_{7/2}$	$4p\ ^4G^o_{9/2}$	1.81E-01	1039	890	

Notes. The f values of Ge IV are from Nath Dutta & Majumder (2011). All Ge V and VI wavelengths are calculated from energy levels in Tables 1 and 3 unless otherwise mentioned in the comment column.

increased C abundance would strengthen C IV lines as well, e.g. C IV $\lambda\lambda$ 948.09, 948.21 Å (Fig. 3), this is evidence that $T_{\rm eff}$ of the model is too high and/or $\log g$ is too low. A respective variation would change the C III/C IV ionization equilibrium towards the lower ionization and improve the agreement of the C III lines. Figures 4 and 5 demonstrate this for $T_{\rm eff} = 70$ kK and $T_{\rm eff} = 65$ kK. We compared theoretical He I, He II, C III, C IV, O IV, and O V line profiles with FUSE and GHRS UV observations and optical UVES observations. The most prominent C III λ 977.020 Å has a strong, blue-shifted interstellar component and is not well suited to an analysis. The better agreement of C III $\lambda\lambda$ 1175 Å in the line cores favors $T_{\rm eff} = 65$ kK, while the "shoulders" between the C III $\lambda\lambda$ 1175 Å components are better matched at $T_{\rm eff} = 70$ kK. The lower $T_{\rm eff}$ is supported by the Ge IV/Ge V ionization balance (Fig. 6), if we judge e.g. Ge IV λ 936.765 Å. The Ge V lines appear almost with same strengths in both ($T_{\rm eff} = 70$ kK and $T_{\rm eff} = 65$ kK) models. On the other hand, Kr VI/Kr VII favors $T_{\rm eff} = 70$ kK (Werner et al. 2012), and He I λ 4471 Å is too strong in the model at $T_{\rm eff} = 65$ kK (Fig. 6). The O IV/O V ionization appears unchanged between $T_{\rm eff} = 65$ kK and $T_{\rm eff} = 70$ kK.

It is worthwhile mentioning that a lower $T_{\rm eff}$ would strongly improve the agreement between model and the observed EUV flux (EUVE J0503−28.8, Werner et al. 2001). A more precise determination of $T_{\rm eff}$ and $\log g$ of RE 0503−289 based on additional high-signal-to-noise ratio (S/N) optical spectra and more ionization equilibria of different species is highly desirable. Our test calculations have shown that our Ge line identifications and abundance determination are affected only marginally by this uncertainty in atmosphere parameters.

6. Results and conclusions

Successful reproduction of the identified Ge lines in high-resolution UV spectra of RE 0503−289 by our synthetic spectra calculated from NLTE model atmospheres using newly calculated oscillator strengths of Ge V and Ge VI shows that – when done with sufficient care – theory works.

We derive a photospheric abundance of $\log {\rm Ge} = -3.8 \pm 0.3$ (mass fraction) in RE 0503−289. This is about 650 times the solar abundance. This high value is similar to the results of Werner et al. (2012) for Kr (450 times solar) and Xe (3800 times solar).

The identifications of trans-iron elements in the FUSE spectrum of RE 0503−289 and the abundance determinations of Ge, Kr, and Xe show that RE 0503−289 is important for our understanding of the non-DA white dwarf evolutionary channel. Further abundance determinations of the identified species is highly desirable. This is a challenge for atomic physicists.

It is worthwhile mentioning here the two HST observations of RE 0503−289 taken with STIS[16] (1999-03-23, ObsIds O56401010, O56401020) that missed the star because the prior target acquisition apparently failed. Unfortunately, they were not repeated. The available GHRS[17] observations cover only small wavelength sections of the NUV, and the IUE high-resolution spectra (e.g. SWP52803HL) have too-low an S/N. Obtaining high-resolution, high S/N spectra with HST/STIS should not be missed because the NUV spectrum probably offers important, additional spectral information.

The Ge model ions that were used in this analysis were developed in the framework of the Virtual Observatory (VO[18]) in a German Astrophysical Virtual Observatory (GAVO[19]) project and are provided within TMAD (Sect. 4). The spectral energy distribution of our final model can be retrieved in VO-compliant form via the registered VO service TheoSSA[20].

Acknowledgements. T.R. is supported by the German Aerospace Center (DLR, grant 05 OR 0806). Financial support from the Belgian FRS-FNRS is also acknowledged. E.B. and P.Q. are Research Director and Senior Research Associate, respectively, of this organization. This research has made use of the SIMBAD database, operated at the CDS, Strasbourg, France. We thank Ralf Napiwotzki for providing us the SPY spectrum of RE 0503−289. Some of the data presented in this paper were obtained from the Mikulski Archive for Space Telescopes (MAST). STScI is operated by the Association of Universities for Research in Astronomy, Inc., under NASA contract NAS5-26555. Support for MAST for non-HST data is provided by the NASA Office of Space Science via grant NNX09AF08G and by other grants and contracts.

References

Biémont, E., & Hansen, J. E. 1989, Phys. Scr., 39, 308
Churilov, S. S., Joshi, Y. N., Ryabtsev, A. N., & Hanlon, M. 1997, Phys. Scr., 55, 54
Cowan, R. D. 1981, The theory of atomic structure and spectra (Berkeley, CA: University of California Press)
Grant, I. P., & McKenzie, B. J. 1980, J. Phys. B At. Mol. Phys., 13, 2671
Grant, I. P., McKenzie, B. J., Norrington, P. H., Mayers, D. F., & Pyper, N. C. 1980, Comp. Phys. Comm., 21, 207
Hamasha, S. M., Shlyaptseva, A. S., & Safronova, U. I. 2004, Can. J. Phys., 82, 331
Holberg, J. B., Barstow, M. A., & Sion, E. M. 1998, ApJS, 119, 207
Jucys, A., Vizbaraite, J., & Karazija, R. 1968, Liet. Fiz. Rinkinys, 8, 551
Napiwotzki, R., Christlieb, N., Drechsel, H., et al. 2001, Astron. Nachr., 322, 411
Napiwotzki, R., Christlieb, N., Drechsel, H., et al. 2003, The Messenger, 112, 25
Nath Dutta, N., & Majumder, S. 2011, ApJ, 737, 25
Quinet, P., & Biémont, E. 1990, Bull. Soc. R. Sci. Liège, 59, 307
Quinet, P., & Biémont, E. 1991, Phys. Scr., 43, 150
Rauch, T., & Deetjen, J. L. 2003, in Stellar Atmosphere Modeling, eds. I. Hubeny, D. Mihalas, & K. Werner, ASP Conf. Ser., 288, 103
Safronova, U. I., & Safronova, A. S. 2006, J. Plasma Fusion Res. Ser., 7, 278
Safronova, U. I., Johnson, W. R., & Albritton, J. R. 2000, Phys. Rev. A, 62, 052505
Safronova, U. I., Safronova, A. S., & Beiersdorfer, P. 2006a, J. Phys. B At. Mol. Phys. Opt., 39, 4491
Safronova, U. I., Safronova, A. S., Hamasha, S. M., & Beiersdorfer, P. 2006b, Atomic Data and Nuclear Data Tables, 92, 47
Savitzky, A., & Golay, M. J. E. 1964, Anal. Chem., 36, 1627
Seaton, M. J. 1962, in Atomic and Molecular Processes, ed. D. R. Bates, 375
Sugar, J., & Musgrove, A. 1993, J. Phys. Chem. Ref. Data, 22, 1213
van Regemorter, H. 1962, ApJ, 136, 906
Werner, K., Deetjen, J. L., Rauch, T., & Wolff, B. 2001, in 12th European Workshop on White Dwarfs, eds. J. L. Provencal, H. L. Shipman, J. MacDonald, & S. Goodchild, ASP Conf. Ser., 226, 55
Werner, K., Deetjen, J. L., Dreizler, S., et al. 2003, in Stellar Atmosphere Modeling, eds. I. Hubeny, D. Mihalas, & K. Werner, ASP Conf. Ser., 288, 31
Werner, K., Rauch, T., Ringat, E., & Kruk, J. W. 2012, ApJ, 753, L7

Pages 7 to 13 are available in the electronic edition of the journal at http://www.aanda.org

[16] Space Telescope Imaging Spectrograph.
[17] Goddard High Resolution Spectrograph.
[18] http://www.ivoa.net/
[19] http://www.g-vo.org
[20] http://dc.g-vo.org/theossa

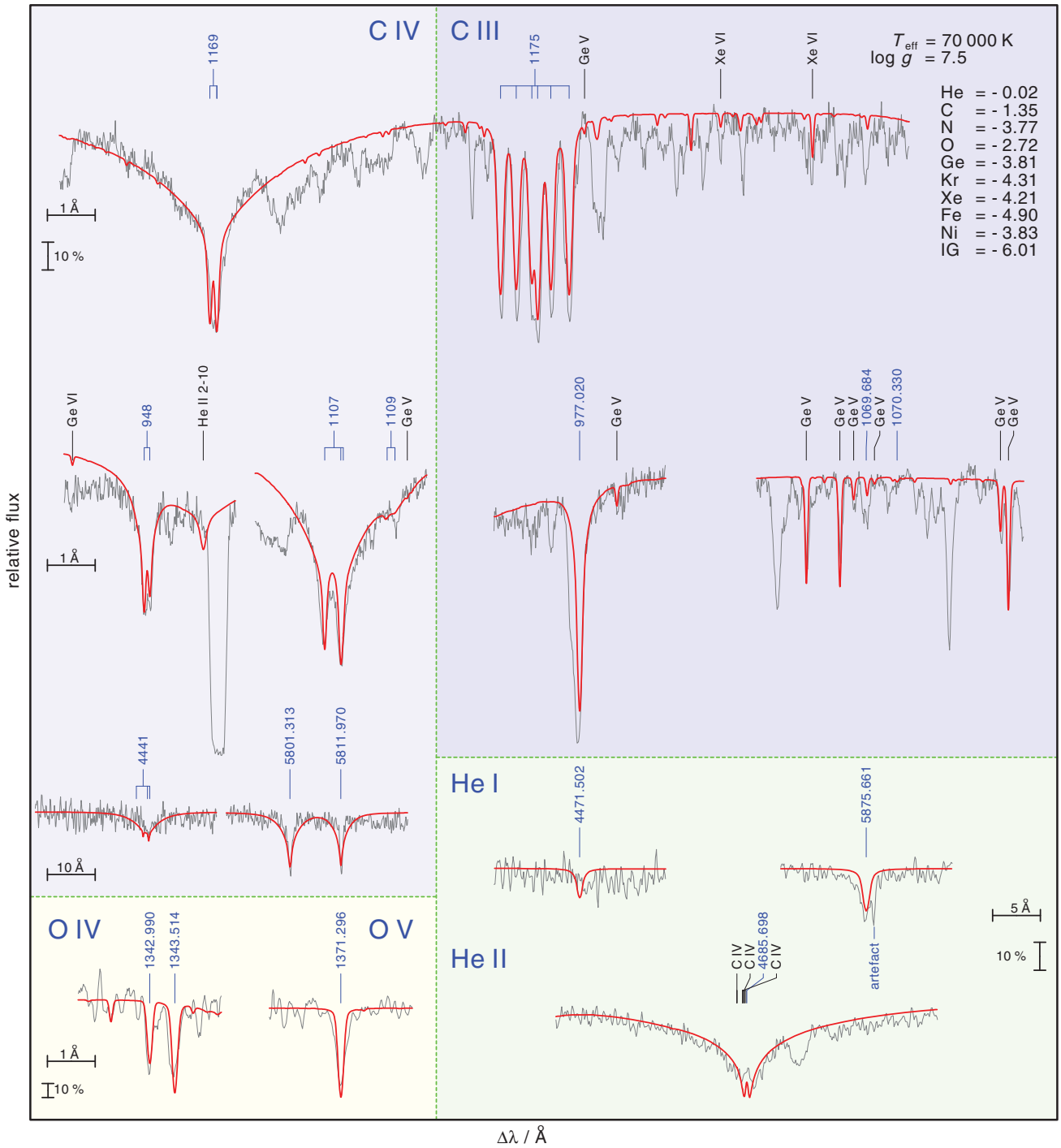

Fig. 4. He I / He II, C III / C IV, and O IV / O V ionization equilibria in our $T_{\rm eff}$ = 70 kK model compared with FUSE, GHRS (smoothed with a low-pass filter (m = 15, n = 4) for clarity, Savitzky & Golay 1964), and UVES observations. Wavelength and flux scales are indicated by bars. The model spectrum is convolved with a Gaussian to match the respective instrument's resolution. Unidentified lines in the model stem from Ca-Ni.

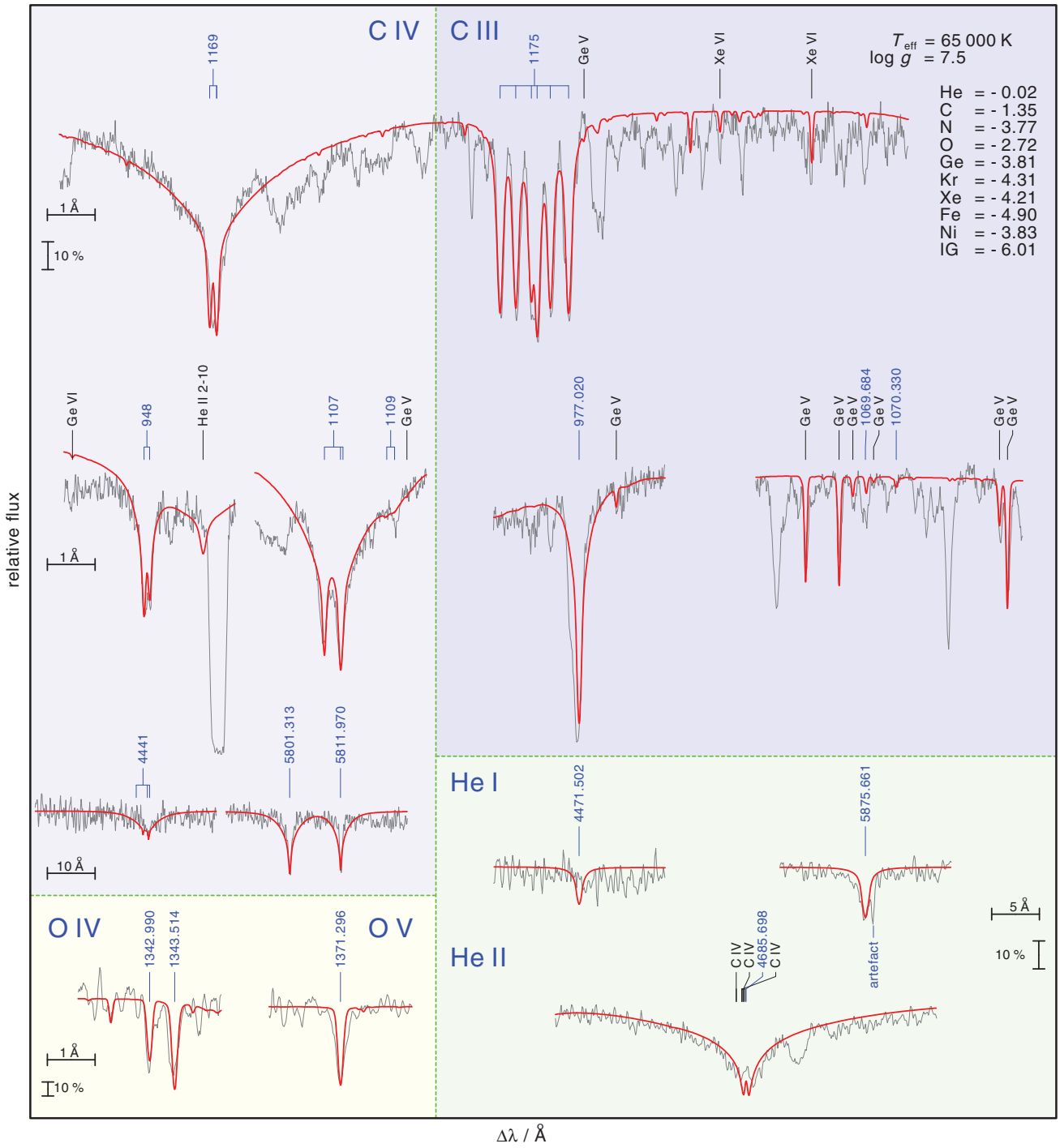

Fig. 5. Same as Fig. 4 for $T_{\rm eff}$ = 65 kK.

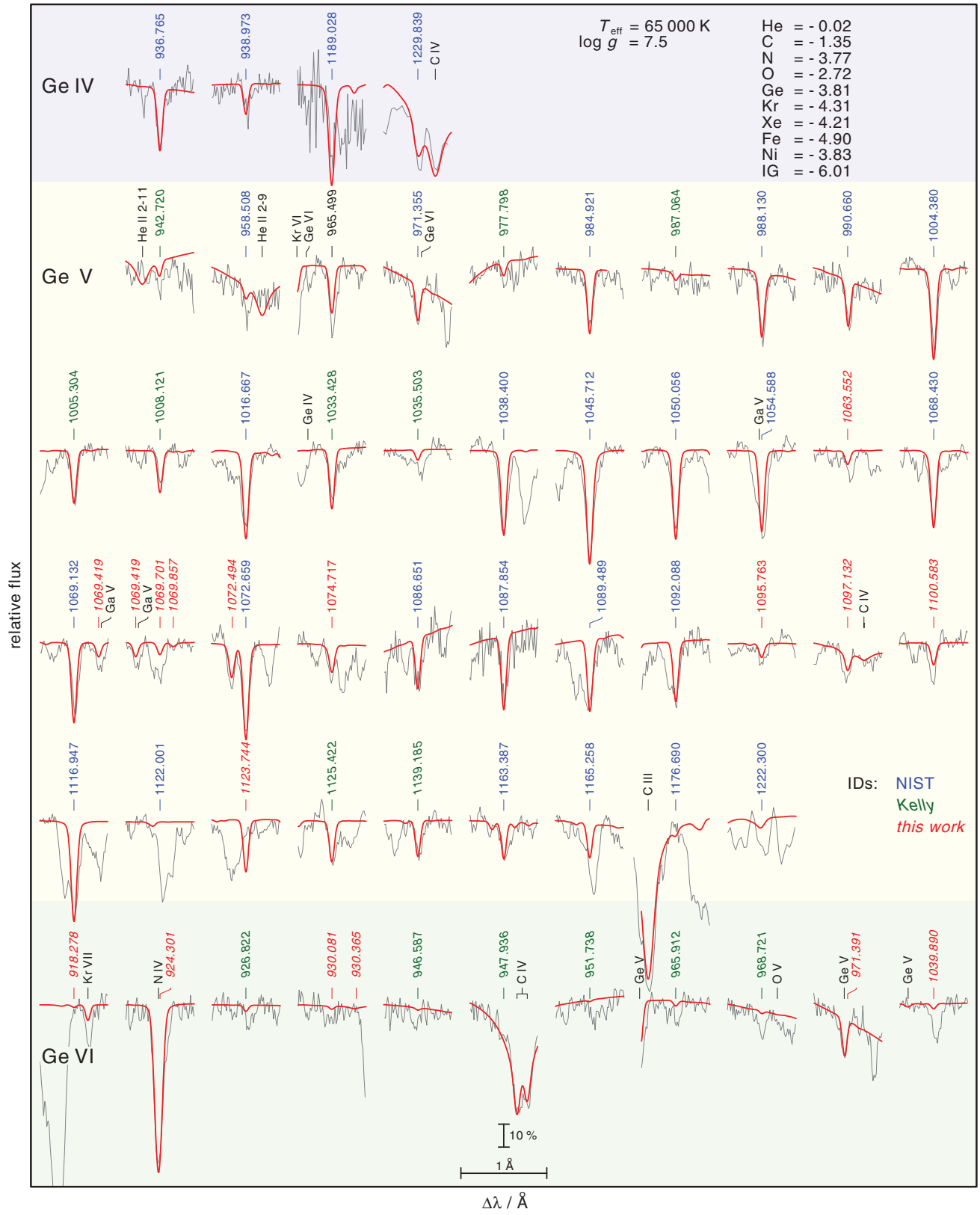

Fig. 6. Same as Fig. 3 for $T_{\rm eff}$ = 65 kK.

Table 1. Energy levels of Ge V (in cm^{-1}). The first three LS-components are given when they are over 5%.

E_{exp}	E_{calc}	ΔE	J	LS-coupling composition (%)
0.0	0	0	0	99 $3d^{10}\ ^1S$
234 219.3	23 4226	–7	3	99 $3d^9 4s\ ^3D$
235 967.0	235 958	9	2	83 $3d^9 4s\ ^3D$
238 764.9	238 765	–4	1	99 $3d^9 4s\ ^3D$
241 935.2	241 937	–2	2	83 $3d^9 4s\ ^1D$
323 748.9	323 877	–128	2	96 $3d^9 4p\ ^3P^\circ$
327 753.0	327 889	–136	1	96 $3d^9 4p\ ^3P^\circ$
327 891.0	327 792	99	3	68 $3d^9 4p\ ^3F^\circ$ + 27 $3d^9 4p\ ^1F^\circ$
329 847.8	329 698	150	4	99 $3d^9 4p\ ^3F^\circ$
330 332.5	330 250	83	0	99 $3d^9 4p\ ^3P^\circ$
330 790.6	330 735	56	2	94 $3d^9 4p\ ^3F^\circ$
335 161.3	335 214	–52	3	60 $3d^9 4p\ ^1F^\circ$ + 27 $3d^9 4p\ ^3D^\circ$ + 12 $3d^9 4p\ ^3F^\circ$
335 560.3	335 621	–61	2	63 $3d^9 4p\ ^1D^\circ$ + 32 $3d^9 4p\ ^3D^\circ$
337 168.1	337 131	37	3	68 $3d^9 4p\ ^3D^\circ$ + 19 $3d^9 4p\ ^3F^\circ$ + 13 $3d^9 4p\ ^1F^\circ$
338 273.5	338 268	5	1	75 $3d^9 4p\ ^1P^\circ$ + 24 $3d^9 4p\ ^3D^\circ$
339 540.2	339 552	–12	1	73 $3d^9 4p\ ^3D^\circ$ + 23 $3d^9 4p\ ^1P^\circ$
340 295.7	340 337	–42	2	60 $3d^9 4p\ ^3D^\circ$ + 36 $3d^9 4p\ ^1D^\circ$
456 051.8	456 107	–55	1	92 $3d^9 4d\ ^3S$ + 6 $3d^9 4d\ ^3P$
461 417.5	461 286	131	5	99 $3d^9 4d\ ^3G$
461 642.6	461 607	36	4	64 $3d^9 4d\ ^3G$ + 34 $3d^9 4d\ ^1G$
461 814.9	461 908	–93	1	50 $3d^9 4d\ ^1P$ + 30 $3d^9 4d\ ^3P$ + 19 $3d^9 4d\ ^3D$
461 828.5	461 834	–6	2	78 $3d^9 4d\ ^3P$ + 21 $3d^9 4d\ ^3D$
463 361.6	463 383	–21	3	85 $3d^9 4d\ ^3D$ + 11 $3d^9 4d\ ^3F$
463 957.9	463 958	0	0	99 $3d^9 4d\ ^3P$
464 077.0	464 020	57	3	63 $3d^9 4d\ ^3G$ + 21 $3d^9 4d\ ^1F$ + 11 $3d^9 4d\ ^3F$
464 652.2	464 660	–7	2	51 $3d^9 4d\ ^3D$ + 23 $3d^9 4d\ ^1D$ + 13 $3d^9 4d\ ^3P$
464 705.7	464 754	–49	4	52 $3d^9 4d\ ^3F$ + 35 $3d^9 4d\ ^1G$ + 12 $3d^9 4d\ ^3G$
464 852.7	464 848	4	1	55 $3d^9 4d\ ^3P$ + 37 $3d^9 4d\ ^1P$ + 7 $3d^9 4d\ ^3S$
466 780.2	466 778	2	3	38 $3d^9 4d\ ^1F$ + 34 $3d^9 4d\ ^3G$ + 27 $3d^9 4d\ ^3F$
467 029.1	466 994	35	1	81 $3d^9 4d\ ^3D$ + 11 $3d^9 4d\ ^1P$ + 8 $3d^9 4d\ ^3P$
467 386.7	467 371	16	4	46 $3d^9 4d\ ^3F$ + 30 $3d^9 4d\ ^1G$ + 23 $3d^9 4d\ ^3G$
468 695.8	468 676	20	2	33 $3d^9 4d\ ^1D$ + 31 $3d^9 4d\ ^3F$ + 28 $3d^9 4d\ ^3D$
469 686.4	469 746	–59	3	50 $3d^9 4d\ ^3F$ + 40 $3d^9 4d\ ^1F$ + 9 $3d^9 4d\ ^3D$
469 889.6	469 901	–12	2	56 $3d^9 4d\ ^3F$ + 43 $3d^9 4d\ ^1D$
490 741.7	490 744	–2	3	100 $3d^9 5s\ ^3D$
491 443.3	491 441	2	2	55 $3d^9 5s\ ^3D$ + 45 $3d^9 5s\ ^1D$
495 288.4	495 287	1	1	100 $3d^9 5s\ ^3D$
495 907.7	495 909	–2	2	55 $3d^9 5s\ ^1D$ + 45 $3d^9 5s\ ^3D$
522 959.0	522 993	–34	2	93 $3d^9 5p\ ^3P^\circ$ + 7 $3d^9 5p\ ^3D^\circ$
524 232.0	524 228	4	3	57 $3d^9 5p\ ^3F^\circ$ + 36 $3d^9 5p\ ^1F^\circ$ + 6 $3d^9 5p\ ^3D^\circ$
524 950.0	524 897	53	4	100 $3d^9 5p\ ^3F^\circ$
525 343.0	525 357	–14	1	72 $3d^9 5p\ ^3P^\circ$ + 22 $3d^9 5p\ ^1P^\circ$ + 6 $3d^9 5p\ ^3D^\circ$
526 373.0	526 383	–10	2	41 $3d^9 5p\ ^1D^\circ$ + 30 $3d^9 5p\ ^3D^\circ$ + 26 $3d^9 5p\ ^3F^\circ$
526 902.0	526 908	–6	3	80 $3d^9 5p\ ^3D^\circ$ + 19 $3d^9 5p\ ^1F^\circ$
528 156.0	528 159	–3	0	100 $3d^9 5p\ ^3P^\circ$
528 625.0	528 600	25	2	71 $3d^9 5p\ ^3F^\circ$ + 26 $3d^9 5p\ ^1D^\circ$
529 476.0	529 472	4	1	77 $3d^9 5p\ ^1P^\circ$ + 22 $3d^9 5p\ ^3P$
530 113.0	530 114	–1	3	44 $3d^9 5p\ ^1F^\circ$ + 42 $3d^9 5p\ ^3F^\circ$ + 14 $3d^9 5p\ ^3D^\circ$
530 928.0	530 919	9	1	94 $3d^9 5p\ ^3D^\circ$
531 321.0	531 348	–27	2	60 $3d^9 5p\ ^3D^\circ$ + 33 $3d^9 5p\ ^1D^\circ$
553 910.9	553 895	16	1	88 $3d^9 4f\ ^3P^\circ$ + 10 $3d^9 4f\ ^3D^\circ$
554 370.9	554 374	–3	2	56 $3d^9 4f\ ^3P^\circ$ + 27 $3d^9 4f\ ^3D^\circ$ + 17 $3d^9 4f\ ^1D^\circ$
554 658.0	554 671	–13	6	100 $3d^9 4f\ ^3H^\circ$
554 690.2	554 714	–24	5	53 $3d^9 4f\ ^1H^\circ$ + 47 $3d^9 4f\ ^3H^\circ$
555 298.8	555 305	–6	2	40 $3d^9 4f\ ^1D^\circ$ + 33 $3d^9 4f\ ^3F^\circ$ + 26 $3d^9 4f\ ^3D^\circ$
555 337.1	555 318	19	3	66 $3d^9 4f\ ^3D^\circ$ + 25 $3d^9 4f\ ^3F$ + 8 $3d^9 4f\ ^1F$
555 730.2	555 717	13	1	59 $3d^9 4f\ ^3D^\circ$ + 37 $3d^9 4f\ ^1P^\circ$
555 798.4	555 792	6	4	76 $3d^9 4f\ ^3F^\circ$ + 20 $3d^9 4f\ ^3G^\circ$
555 852.3	555 858	–6	5	79 $3d^9 4f\ ^3G^\circ$ + 11 $3d^9 4f\ ^3H^\circ$ + 11 $3d^9 4f\ ^1H^\circ$
555 860.0	555 862	–2	4	49 $3d^9 4f\ ^1G^\circ$ + 28 $3d^9 4f\ ^3G^\circ$ + 21 $3d^9 4f\ ^3H^\circ$
555 912.7	555 912	1	3	47 $3d^9 4f\ ^1F^\circ$ + 28 $3d^9 4f\ ^3F^\circ$ + 23 $3d^9 4f\ ^3G^\circ$
558 877.1	558 871	6	2	44 $3d^9 4f\ ^3P^\circ$ + 34 $3d^9 4f\ ^3D^\circ$ + 22 $3d^9 4f\ ^1D^\circ$
559 463.1	559 452	11	4	78 $3d^9 4f\ ^3H^\circ$ + 12 $3d^9 4f\ ^1G^\circ$ + 10 $3d^9 4f\ ^3G^\circ$
559 467.6	559 487	–20	5	42 $3d^9 4f\ ^3H^\circ$ + 37 $3d^9 4f\ ^1H^\circ$ + 21 $3d^9 4f\ ^3G^\circ$

Table 1. continued.

E_{exp}	E_{calc}	ΔE	J	LS-coupling composition (%)
560 034.6	560 024	11	2	66 $3d^9 4f\ ^3F^\circ$ + 21 $3d^9 4f\ ^1D^\circ$ + 13 $3d^9 4f\ ^3D^\circ$
560 096.6	560 095	2	3	41 $3d^9 4f\ ^3F^\circ$ + 32 $3d^9 4f\ ^3D^\circ$ + 26 $3d^9 4f\ ^1F^\circ$
560 149.3	560 157	–7	1	60 $3d^9 4f\ ^1P^\circ$ + 30 $3d^9 4f\ ^3D^\circ$ + 9 $3d^9 4f\ ^3P^\circ$
560 547.2	560 559	–12	4	43 $3d^9 4f\ ^3G^\circ$ + 35 $3d^9 4f\ ^1G^\circ$ + 22 $3d^9 4f\ ^3F^\circ$
560 587.7	560 579	9	3	76 $3d^9 4f\ ^3G^\circ$ + 18 $3d^9 4f\ ^1F^\circ$ + 6 $3d^9 4f\ ^3F^\circ$
574 389.0	574 404	–14	1	79 $3d^9 5d\ ^3S$ + 15 $3d^9 5d\ ^3P$
576 067.0	576 047	20	5	100 $3d^9 5d\ ^3G$
576 226.0	576 206	20	4	55 $3d^9 5d\ ^3G$ + 44 $3d^9 5d\ ^1G$
576 963.0	576 934	29	3	84 $3d^9 5d\ ^3D$ + 13 $3d^9 5d\ ^3F$
577 459.0	577 444	15	3	48 $3d^9 5d\ ^1F$ + 29 $3d^9 5d\ ^3F$ + 22 $3d^9 5d\ ^3G$
577 553.0	577 623	–79	4	80 $3d^9 5d\ ^3F$ + 14 $3d^9 5d\ ^1G$
580 695.0	580 724	–29	3	78 $3d^9 5d\ ^3G$ + 14 $3d^9 5d\ ^1F$ + 8 $3d^9 5d\ ^3F$
581 114.0	581 106	8	4	41 $3d^9 5d\ ^1G$ + 40 $3d^9 5d\ ^3G$ + 19 $3d^9 5d\ ^3F$
582 225.0	582 201	24	3	50 $3d^9 5d\ ^3F$ + 36 $3d^9 5d\ ^1F$ + 14 $3d^9 5d\ ^3D$
582 308.0	582 311	–3	2	68 $3d^9 5d\ ^3F$ + 30 $3d^9 5d\ ^1D$
588 094.0	588 095	–1	3	100 $3d^9 6s\ ^3D$
588 403.0	588 402	1	2	54 $3d^9 6s\ ^1D$ + 46 $3d^9 6s\ ^3D$
592 644.0	592 643	1	1	100 $3d^9 6s\ ^3D$
592 872.0	592 873	–1	2	54 $3d^9 6s\ ^3D$ + 46 $3d^9 6s\ ^1D$
601 967.0	602 124	–157	4	76 $3d^8 4s(^4F)4p\ ^5F^\circ$ + 9 $3d^8 4s(^4F)4p\ ^5G^\circ$
603 355.0	603 363	–8	2	90 $3d^9 6p\ ^3P^\circ$ + 9 $3d^9 6p\ ^3D^\circ$
603 929.0	603 934	–5	3	52 $3d^9 6p\ ^3F^\circ$ + 40 $3d^9 6p\ ^1F^\circ$ + 7 $3d^9 6p\ ^3D^\circ$
604 182.0	604 165	17	4	87 $3d^9 6p\ ^3F^\circ$
604 278.0	604 253	25	4	31 $3d^8 4s(^2F)4p\ ^3G^\circ$ + 23 $3d^8 4s(^2F)4p\ ^1G^\circ$ + 15 $3d^8 4s(^4F)4p\ ^3G^\circ$
604 648.0	604 656	–8	1	48 $3d^9 6p\ ^3P^\circ$ + 41 $3d^9 6p\ ^1P^\circ$ + 8 $3d^9 6p\ ^3D^\circ$
604 928.0	604 922	6	3	42 $3d^9 6p\ ^3D^\circ$ + 26 $3d^8 4s(^2F)4p\ ^3D^\circ$ + 11 $3d^8 4s(^4F)4p\ ^3D^\circ$
604 935.0	604 910	25	2	54 $3d^9 6p\ ^1D^\circ$ + 31 $3d^9 6p\ ^3D^\circ$ + 10 $3d^9 6p\ ^3F^\circ$
605 218.0	605 263	–45	3	42 $3d^9 6p\ ^3D^\circ$ + 26 $3d^8 4s(^2F)4p\ ^3D^\circ$ + 8 $3d^9 6p\ ^1F^\circ$
606 815.0	606 769	46	2	47 $3d^8 4s(^2F)4p\ ^3D^\circ$ + 19 $3d^8 4s(^4F)4p\ ^3D^\circ$ + 10 $3d^8 4s(^2F)4p\ ^3F^\circ$
607 097.0	607 108	–11	3	56 $3d^8 4s(^2F)4p\ ^3G^\circ$ + 27 $3d^8 4s(^4F)4p\ ^3G^\circ$ + 6 $3d^8 4s(^2F)4p\ ^3D^\circ$
608 207.0	608 191	16	0	100 $3d^9 6p\ ^3P^\circ$
608 340.0	608 349	–9	2	85 $3d^9 6p\ ^3F^\circ$ + 14 $3d^9 6p\ ^1D^\circ$
608 587.0	608 664	–77	1	54 $3d^9 6p\ ^1P^\circ$ + 46 $3d^9 6p\ ^3P^\circ$
609 075.0	609 063	12	3	47 $3d^9 6p\ ^3F^\circ$ + 43 $3d^9 6p\ ^1F^\circ$ + 9 $3d^9 6p\ ^3D^\circ$
609 083.0	608 951	132	1	42 $3d^8 4s(^2F)4p\ ^3D^\circ$ + 20 $3d^8 4s(^4F)4p\ ^3D^\circ$ + 16 $3d^9 6p\ ^3D^\circ$
609 246.0	609 294	–48	4	53 $3d^8 4s(^2F)4p\ ^3F^\circ$ + 32 $3d^8 4s(^4F)4p\ ^3F^\circ$ + 7 $3d^8 4s(^4F)4p\ ^5F^\circ$
609 501.0	609 531	–30	1	76 $3d^9 6p\ ^3D^\circ$ + 10 $3d^8 4s(^2F)4p\ ^3D^\circ$
609 609.0	609 601	8	2	59 $3d^9 6p\ ^3D^\circ$ + 31 $3d^9 6p\ ^1D^\circ$ + 6 $3d^9 6p\ ^3P^\circ$
609 963.0	609 943	20	3	32 $3d^8 4s(^2F)4p\ ^3F^\circ$ + 23 $3d^8 4s(^2F)4p\ ^1F^\circ$ + 19 $3d^8 4s(^4F)4p\ ^3F^\circ$
611 844.0	611 865	–21	2	49 $3d^8 4s(^2F)4p\ ^3F^\circ$ + 27 $3d^8 4s(^4F)4p\ ^3F^\circ$ + 8 $3d^8 4s(^2F)4p\ ^3D^\circ$
614 161.0	614 129	32	2	66 $3d^8 4s(^2F)4p\ ^1D^\circ$ + 14 $3d^8 4s(^4P)4p\ ^5P^\circ$ + 6 $3d^8 4s(^2D)4p\ ^3P^\circ$
614 754.0	614 750	4	3	51 $3d^8 4s(^2F)4p\ ^1F^\circ$ + 16 $3d^8 4s(^4P)4p\ ^5P^\circ$ + 11 $3d^8 4s(^2D)4p\ ^3D^\circ$
615 820.0	615 814	6	2	70 $3d^8 4s(^4P)4p\ ^5P^\circ$ + 18 $3d^8 4s(^2F)4p\ ^1D^\circ$
617 340.0	617 318	22	1	81 $3d^9 5f\ ^3P^\circ$ + 16 $3d^9 5f\ ^3D^\circ$
618 540.0	618 619	–79	1	54 $3d^9 5f\ ^3D^\circ$ + 39 $3d^9 5f\ ^1P^\circ$ + 7 $3d^9 5f\ ^3P^\circ$
620 940.0	620 955	–15	2	75 $3d^8 4s(^2D)4p\ ^3F^\circ$
621 888.0	621 765	123	3	67 $3d^8 4s(^2D)4p\ ^3F^\circ$ + 7 $3d^8 4s(^4P)4p\ ^5D^\circ$ + 6 $3d^8 4s(^2G)4p\ ^3F^\circ$
622 200.0	622 265	–65	1	44 $3d^8 4s(^2D)4p\ ^3D^\circ$ + 16 $3d^8 4s(^2D)4p\ ^3P^\circ$ + 11 $3d^8 4s(^2F)4p\ ^3D^\circ$
622 627.0	622 572	55	2	58 $3d^9 5f\ ^3F^\circ$ + 19 $3d^9 5f\ ^1D^\circ$ + 14 $3d^9 5f\ ^3D^\circ$
622 759.0	622 566	193	4	34 $3d^8 4s(^2D)4p\ ^3F^\circ$ + 20 $3d^9 5f\ ^3G^\circ$ + 18 $3d^9 5f\ ^1G^\circ$
622 980.0	623 065	–85	1	59 $3d^9 5f\ ^1P^\circ$ + 28 $3d^9 5f\ ^3D^\circ$ + 11 $3d^9 5f\ ^3P^\circ$
623 081.0	623 121	–40	2	52 $3d^8 4s(^2D)4p\ ^3D^\circ$ + 7 $3d^8 4s(^2F)4p\ ^3D^\circ$ + 7 $3d^8 4s(^2D)4p\ ^3F^\circ$
624 057.0	624 159	–102	3	70 $3d^8 4s(^2D)4p\ ^3D^\circ$ + 8 $3d^8 4s(^4P)4p\ ^5P^\circ$
624 684.0	624 678	6	1	41 $3d^8 4s(^2D)4p\ ^3P^\circ$ + 32 $3d^8 4s(^2D)4p\ ^3D^\circ$ + 11 $3d^8 4s(^2P)4p\ ^3P^\circ$
625 990.0	625 902	88	2	67 $3d^8 4s(^2D)4p\ ^3P^\circ$ + 15 $3d^8 4s(^2D)4p\ ^3D^\circ$
626 651.0	626 697	–46	1	86 $3d^8 4s(^4P)4p\ ^5D^\circ$ + 9 $3d^8 4s(^4F)4p\ ^5D^\circ$
627 067.0	626 899	168	2	82 $3d^8 4s(^4P)4p\ ^5D^\circ$ + 7 $3d^8 4s(^4F)4p\ ^5D^\circ$
627 229.0	627 336	–107	3	76 $3d^8 4s(^4P)4p\ ^5D^\circ$ + 8 $3d^8 4s(^2D)4p\ ^3F^\circ$ + 6 $3d^8 4s(^4F)4p\ ^5D^\circ$
627 958.0	627 879	79	4	67 $3d^8 4s(^4P)4p\ ^5D^\circ$ + 17 $3d^8 4s(^2G)4p\ ^3F^\circ$ + 11 $3d^8 4s(^2D)4p\ ^3F^\circ$
630 288.0	630 242	46	2	49 $3d^8 4s(^2P)4p\ ^3P^\circ$ + 16 $3d^8 4s(^4P)4p\ ^3P^\circ$ + 13 $3d^8 4s(^2P)4p\ ^3D^\circ$
631 618.0	631 645	–27	1	34 $3d^8 4s(^2P)4p\ ^3P^\circ$ + 23 $3d^8 4s(^2D)4p\ ^3P^\circ$ + 17 $3d^8 4s(^2P)4p\ ^3D^\circ$
633 144.0	633 168	–24	2	31 $3d^8 4s(^2P)4p\ ^3D^\circ$ + 16 $3d^8 4s(^4P)4p\ ^3D^\circ$ + 12 $3d^8 4s(^2P)4p\ ^3P^\circ$
633 171.0	633 282	–111	1	41 $3d^8 4s(^2P)4p\ ^3D^\circ$ + 19 $3d^8 4s(^4P)4p\ ^3D^\circ$ + 14 $3d^8 4s(^2P)4p\ ^1P^\circ$
633 258.0	633 307	–49	3	36 $3d^8 4s(^2P)4p\ ^3D^\circ$ + 21 $3d^8 4s(^2G)4p\ ^3F^\circ$ + 20 $3d^8 4s(^2P)4p\ ^3D^\circ$

Table 1. continued.

E_{exp}	E_{calc}	ΔE	J	LS-coupling composition (%)
633 570.0	633 575	–5	0	45 $3d^8 4s(^2P)4p\ ^3P^\circ$ + 40 $3d^8 4s(^2D)4p\ ^3P^\circ$ + 10 $3d^8 4s(^4P)4p\ ^3P^\circ$
634 154.0	634 294	–140	4	54 $3d^8 4s(^2G)4p\ ^3F^\circ$ + 21 $3d^8 4s(^2D)4p\ ^3F^\circ$ + 11 $3d^8 4s(^2F)4p\ ^3F^\circ$
635 602.0	635 662	–60	3	51 $3d^8 4s(^2G)4p\ ^3F^\circ$ + 14 $3d^8 4s(^2D)4p\ ^3F^\circ$ + 13 $3d^8 4s(^2P)4p\ ^3D^\circ$
635 973.0	635 974	–1	3	100 $3d^9 7s\ ^3D$
636 143.0	636 142	1	2	57 $3d^9 7s\ ^1D$ + 43 $3d^9 7s\ ^3D$
636 503.0	636 291	212	2	70 $3d^8 4s(^2G)4p\ ^3F^\circ$ + 8 $3d^8 4s(^2D)4p\ ^3F^\circ$ + 7 $3d^8 4s(^2F)4p\ ^3F^\circ$
637 786.0	637 827	–41	3	56 $3d^8 4s(^4F)4p\ ^3D^\circ$ + 19 $3d^8 4s(^2F)4p\ ^3D^\circ$ + 10 $3d^8 4s(^4P)4p\ ^3D^\circ$
638 636.0	638 740	–104	4	38 $3d^8 4s(^4F)4p\ ^3G^\circ$ + 23 $3d^8 4s(^2F)4p\ ^3G^\circ$ + 18 $3d^8 4s(^4F)4p\ ^3F^\circ$
640 509.0	640 508	1	1	100 $3d^9 7s\ ^3D$
640 625.0	640 626	–1	2	57 $3d^9 7s\ ^3D$ + 43 $3d^9 7s\ ^1D$
640 855.0	640 666	189	4	36 $3d^8 4s(^4F)4p\ ^3F^\circ$ + 20 $3d^8 4s(^4F)4p\ ^3G^\circ$ + 19 $3d^8 4s(^2F)4p\ ^3F^\circ$
641 390.0	641 392	–2	2	56 $3d^8 4s(^4F)4p\ ^3D^\circ$ + 22 $3d^8 4s(^2F)4p\ ^3D^\circ$ + 8 $3d^8 4s(^4P)4p\ ^3D^\circ$
643 477.0	643 461	16	1	56 $3d^8 4s(^4F)4p\ ^3D^\circ$ + 24 $3d^8 4s(^2F)4p\ ^3D^\circ$ + 7 $3d^8 4s(^4P)4p\ ^3D^\circ$
643 724.0	643 609	115	3	45 $3d^8 4s(^4F)4p\ ^3F^\circ$ + 23 $3d^8 4s(^2F)4p\ ^3F^\circ$ + 6 $3d^8 4s(^2F)4p\ ^3G^\circ$
645 100.0	645 113	–13	2	31 $3d^9 7p\ ^1D^\circ$ + 26 $3d^8 4s(^4F)4p\ ^3F^\circ$ + 15 $3d^9 7p\ ^3P^\circ$
645 761.0	645 779	–18	2	31 $3d^8 4s(^4F)4p\ ^3F^\circ$ + 28 $3d^9 7p\ ^1D^\circ$ + 15 $3d^8 4s(^2F)4p\ ^3P^\circ$
649 365.0	649 363	2	1	55 $3d^9 7p\ ^3P^\circ$ + 44 $3d^9 7p\ ^1P^\circ$
652 760.0	652 759	1	1	48 $3d^9 6f\ ^3D^\circ$ + 44 $3d^9 6f\ ^1P^\circ$ + 7 $3d^9 6f\ ^3P^\circ$
657 140.0	657 136	4	1	53 $3d^9 6f\ ^1P^\circ$ + 32 $3d^9 6f\ ^3D^\circ$ + 14 $3d^9 6f\ ^3P^\circ$
658 225.0	658 292	–67	2	44 $3d^8 4s(^2D)4p\ ^1D^\circ$ + 29 $3d^8 4s(^4P)4p\ ^3P^\circ$ + 11 $3d^8 4s(^2P)4p\ ^3P^\circ$
660 117.0	660 121	–4	1	44 $3d^8 4s(^4P)4p\ ^3P^\circ$ + 29 $3d^8 4s(^2D)4p\ ^1P^\circ$ + 15 $3d^8 4s(^2P)4p\ ^3P^\circ$
662 544.0	662 506	38	0	71 $3d^8 4s(^4P)4p\ ^3P^\circ$ + 23 $3d^8 4s(^2P)4p\ ^3P^\circ$
662 890.0	662 996	–106	2	37 $3d^8 4s(^2D)4p\ ^1P^\circ$ + 41 $3d^8 4s(^2D)4p\ ^1D^\circ$ + 15 $3d^8 4s(^2P)4p\ ^3P^\circ$
664 749.0	664 753	–4	1	55 $3d^8 4s(^2D)4p\ ^1P^\circ$ + 26 $3d^8 4s(^2P)4p\ ^3P^\circ$ + 9 $3d^8 4s(^2P)4p\ ^3P^\circ$
665 937.0	665 832	105	3	44 $3d^8 4s(^4G)4p\ ^3D^\circ$ + 31 $3d^8 4s(^2P)4p\ ^3D^\circ$ + 14 $3d^8 4s(^2D)4p\ ^1F^\circ$
672 445.0	672 521	–76	3	87 $3d^8 4s(^2G)4p\ ^1F^\circ$ + 7 $3d^8 4s(^2D)4p\ ^1F^\circ$
683 090.0	683 102	–12	0	96 $3d^8 4s(^2S)4p\ ^3P^\circ$
684 337.0	684 227	110	1	96 $3d^8 4s(^2S)4p\ ^3P^\circ$
686 617.0	686 716	–99	2	97 $3d^8 4s(^2S)4p\ ^3P^\circ$

Table 3. Energy levels of Ge VI (in cm^{-1}). The first three LS-components are given when they are over 5%.

E_{exp}	E_{calc}	ΔE	J	LS-coupling composition (%)
0.0	0	0	2.5	99 $3d^9\ ^2D$
4560.0	4560	0	1.5	99 $3d^9\ ^2D$
303 696.2	303 702	–6	4.5	99 $3d^8(^3F)4s\ ^4F$
306 243.4	306 227	17	3.5	93 $3d^8(^3F)4s\ ^4F$ + 7 $3d^8(^3F)4s\ ^2F$
308 657.2	308 619	38	2.5	97 $3d^8(^3F)4s\ ^4F$
310 199.1	310 149	50	1.5	97 $3d^8(^3F)4s\ ^4F$
313 024.6	313 083	–59	3.5	93 $3d^8(^3F)4s\ ^2F$ + 7 $3d^8(^3F)4s\ ^4F$
316 936.8	316 978	–41	2.5	94 $3d^8(^3F)4s\ ^2F$
327 537.9	327 580	–42	2.5	52 $3d^8(^3P)4s\ ^4P$ + 45 $3d^8(^1D)4s\ ^2D$
329 073.6	328 991	83	1.5	74 $3d^8(^1D)4s\ ^2D$ + 17 $3d^8(^3P)4s\ ^4P$ + 7 $3d^8(^3P)4s\ ^2P$
332 376.6	332 399	–22	1.5	82 $3d^8(^3P)4s\ ^4P$ + 17 $3d^8(^1D)4s\ ^2D$
332 497.0	332 529	–32	0.5	99 $3d^8(^3P)4s\ ^4P$
333 034.6	333 108	–73	2.5	50 $3d^8(^1D)4s\ ^2D$ + 48 $3d^8(^3P)4s\ ^4P$
339 335.3	339 356	–21	1.5	92 $3d^8(^3P)4s\ ^2P$ + 7 $3d^8(^1D)4s\ ^2D$
340 525.3	340 418	107	0.5	99 $3d^8(^3P)4s\ ^2P$
343 624.4	343 641	–16	4.5	99 $3d^8(^1G)4s\ ^2G$
343 674.0	343 658	16	3.5	99 $3d^8(^1G)4s\ ^2G$
391 183.2	391 183	0	0.5	99 $3d^8(^1S)4s\ ^2S$
404 892.3	405 152	–260	3.5	87 $3d^8(^3F)4p\ ^4D^\circ$ + 6 $3d^8(^3F)4p\ ^4F^\circ$
408 981.1	409 123	–142	2.5	85 $3d^8(^3F)4p\ ^4D^\circ$ + 7 $3d^8(^3F)4p\ ^4F^\circ$ + 6 $3d^8(^3P)4p\ ^4D^\circ$
409 188.4	409 218	–30	4.5	56 $3d^8(^3F)4p\ ^4G^\circ$ + 25 $3d^8(^3F)4p\ ^2G^\circ$ + 18 $3d^8(^3F)4p\ ^4F^\circ$
411 591.6	411 314	278	5.5	99 $3d^8(^3F)4p\ ^4G^\circ$
411 885.9	411 737	149	3.5	76 $3d^8(^3F)4p\ ^4G^\circ$ + 12 $3d^8(^3F)4p\ ^4F^\circ$ + 9 $3d^8(^3F)4p\ ^2G^\circ$
412 037.7	412 098	–60	1.5	87 $3d^8(^3F)4p\ ^4D^\circ$ + 8 $3d^8(^3P)4p\ ^4D^\circ$
413 728.0	413 500	228	2.5	88 $3d^8(^3F)4p\ ^4G^\circ$ + 7 $3d^8(^3F)4p\ ^4F^\circ$
413 872.6	413 887	–14	0.5	89 $3d^8(^3F)4p\ ^4D^\circ$ + 10 $3d^8(^3P)4p\ ^4D^\circ$
415 142.7	415 074	69	4.5	79 $3d^8(^3F)4p\ ^4F^\circ$ + 14 $3d^8(^3F)4p\ ^2G^\circ$ + 7 $3d^8(^3F)4p\ ^4G^\circ$
416 709.7	416 633	77	3.5	58 $3d^8(^3F)4p\ ^4F^\circ$ + 25 $3d^8(^3F)4p\ ^2F^\circ$ + 9 $3d^8(^3F)4p\ ^4G^\circ$
417 421.2	417 416	5	4.5	61 $3d^8(^3F)4p\ ^2G^\circ$ + 37 $3d^8(^3F)4p\ ^4G^\circ$
417 792.2	417 828	–36	1.5	64 $3d^8(^3F)4p\ ^4F^\circ$ + 20 $3d^8(^3F)4p\ ^2D^\circ$ + 11 $3d^8(^1D)4p\ ^2D^\circ$
417 941.9	417 861	81	2.5	63 $3d^8(^3F)4p\ ^4F^\circ$ + 19 $3d^8(^3F)4p\ ^2D^\circ$ + 7 $3d^8(^3F)4p\ ^4G^\circ$
420 117.8	420 255	–137	2.5	60 $3d^8(^3F)4p\ ^2D^\circ$ + 15 $3d^8(^3F)4p\ ^2F^\circ$ + 13 $3d^8(^3F)4p\ ^4F^\circ$
420 542.0	420 655	–113	3.5	58 $3d^8(^3F)4p\ ^2F^\circ$ + 21 $3d^8(^3F)4p\ ^2G^\circ$ + 19 $3d^8(^3F)4p\ ^4F^\circ$
421 310.0	421 376	–66	3.5	66 $3d^8(^3F)4p\ ^2G^\circ$ + 13 $3d^8(^3F)4p\ ^2F^\circ$ + 13 $3d^8(^3F)4p\ ^4G^\circ$
423 030.0	423 105	–75	1.5	54 $3d^8(^3F)4p\ ^2D^\circ$ + 30 $3d^8(^3F)4p\ ^4F^\circ$ + 9 $3d^8(^1D)4p\ ^2D^\circ$
424 506.4	424 513	–7	2.5	74 $3d^8(^3F)4p\ ^2F^\circ$ + 12 $3d^8(^3F)4p\ ^2D^\circ$ + 9 $3d^8(^3F)4p\ ^4F^\circ$
429 997.3	430 095	–98	1.5	73 $3d^8(^3P)4p\ ^4P^\circ$ + 9 $3d^8(^1D)4p\ ^2P^\circ$ + 8 $3d^8(^3F)4p\ ^2D^\circ$
430 736.0	430 846	–110	2.5	65 $3d^8(^3P)4p\ ^4P^\circ$ + 12 $3d^8(^1D)4p\ ^2D^\circ$ + 11 $3d^8(^1D)4p\ ^2F^\circ$
431 041.9	431 094	–52	0.5	91 $3d^8(^3P)4p\ ^4P^\circ$
433 507.0	433 438	69	2.5	69 $3d^8(^1D)4p\ ^2F^\circ$ + 20 $3d^8(^3P)4p\ ^4P^\circ$
436 023.6	436 071	–47	1.5	43 $3d^8(^1D)4p\ ^2D^\circ$ + 18 $3d^8(^3P)4p\ ^4P^\circ$ + 15 $3d^8(^1D)4p\ ^2P^\circ$
436 173.3	435 966	207	3.5	71 $3d^8(^1D)4p\ ^2F^\circ$ + 13 $3d^8(^1G)4p\ ^2F^\circ$ + 11 $3d^8(^3P)4p\ ^4D^\circ$
436 727.0	436 699	28	0.5	60 $3d^8(^1D)4p\ ^2P^\circ$ + 28 $3d^8(^3P)4p\ ^2P^\circ$ + 7 $3d^8(^3P)4p\ ^4P^\circ$
437 801.0	437 951	–150	2.5	74 $3d^8(^1D)4p\ ^2D^\circ$ + 8 $3d^8(^3P)4p\ ^4P^\circ$ + 7 $3d^8(^3P)4p\ ^2D^\circ$
438 871.4	438 918	–46	1.5	49 $3d^8(^1D)4p\ ^2P^\circ$ + 31 $3d^8(^1D)4p\ ^2D^\circ$ + 6 $3d^8(^3P)4p\ ^2P^\circ$
441 221.0	441 056	165	0.5	86 $3d^8(^3P)4p\ ^4D^\circ$ + 9 $3d^8(^3F)4p\ ^4D^\circ$
441 278.0	441 101	177	1.5	74 $3d^8(^3P)4p\ ^4D^\circ$ + 6 $3d^8(^3F)4p\ ^4D^\circ$ + 6 $3d^8(^1D)4p\ ^2P^\circ$
441 386.0	441 368	18	2.5	60 $3d^8(^3P)4p\ ^4D^\circ$ + 18 $3d^8(^3P)4p\ ^2D^\circ$ + 6 $3d^8(^1D)4p\ ^2F^\circ$
442 790.4	442 667	123	3.5	76 $3d^8(^3P)4p\ ^4D^\circ$ + 15 $3d^8(^1G)4p\ ^2F^\circ$
444 442.2	444 429	13	4.5	97 $3d^8(^1G)4p\ ^2H^\circ$
445 439.0	445 313	126	1.5	74 $3d^8(^3P)4p\ ^2P^\circ$ + 12 $3d^8(^1D)4p\ ^2P^\circ$ + 7 $3d^8(^3P)4p\ ^2D^\circ$
445 670.0	445 783	–113	2.5	67 $3d^8(^3P)4p\ ^2D^\circ$ + 25 $3d^8(^3P)4p\ ^4D^\circ$
447 373.0	447 431	–58	1.5	83 $3d^8(^3P)4p\ ^2D^\circ$ + 9 $3d^8(^3P)4p\ ^4D^\circ$
447 780.0	447 962	–182	3.5	66 $3d^8(^1G)4p\ ^2F^\circ$ + 21 $3d^8(^1D)4p\ ^2F^\circ$ + 7 $3d^8(^3P)4p\ ^4D^\circ$
448 258.9	448 097	162	5.5	99 $3d^8(^1G)4p\ ^2H^\circ$
449 093.0	448 900	193	0.5	60 $3d^8(^3P)4p\ ^2P^\circ$ + 23 $3d^8(^1D)4p\ ^2P^\circ$ + 13 $3d^8(^3P)4p\ ^2S^\circ$
450 153.0	450 186	–33	2.5	84 $3d^8(^1G)4p\ ^2F^\circ$ + 8 $3d^8(^1D)4p\ ^2F^\circ$
451 362.0	451 604	–242	0.5	84 $3d^8(^3P)4p\ ^2S^\circ$ + 8 $3d^8(^1D)4p\ ^2P^\circ$ + 6 $3d^8(^3P)4p\ ^2P^\circ$
451 501.0	451 538	–37	1.5	96 $3d^8(^3P)4p\ ^4S^\circ$
458 378.0	458 402	–24	3.5	96 $3d^8(^1G)4p\ ^2G^\circ$
459 014.5	459 053	–39	4.5	97 $3d^8(^1G)4p\ ^2G^\circ$
496 179.5	496 213	–33	0.5	97 $3d^8(^1S)4p\ ^2P^\circ$
500 575.3	500 541	34	1.5	97 $3d^8(^1S)4p\ ^2P^\circ$